Journal of Materials Chemistry A

COMMUNICATION

View Article Online
View Journal | View Issue

Cite this: J. Mater. Chem. A, 2017, 5, 3167

Received 28th November 2016
Accepted 24th January 2017

DOI: 10.1039/c6ta10222k

rsc.li/materials-a

Band-aligned $C_3N_{4-x}S_{3x/2}$ stabilizes CdS/$CuInGaS_2$ photocathodes for efficient water reduction†

Danping Wang,[a] Chongwu Wang,[b] F. Pelayo García de Arquer,[c] Juhua Zhong,*[a] Ling Qian,[b] Lijun Fang,[b] Pengfei Liu,[b] Yuanjie Pang,[d] Min Liu,[c] Mengxia Liu,[c] Gengfeng Zheng,[e] David Sinton,[d] Edward H. Sargent,[c] Huagui Yang[b] and Bo Zhang*[ac]

Compared with bare CIGS films and CdS-modified CIGS films (CdS/CIGS), $C_3N_{4-x}S_{3x/2}$/CdS/CIGS electrodes exhibit a reduction of 200 mV in the onset potential. They also show a doubled photocurrent at 0 V *versus* the RHE, and a broadband 20% enhancement of incident photon to current efficiency (IPCE) in noble-metal-free systems. Remarkably, the $C_3N_{4-x}S_{3x/2}$/CdS/CIGS electrode shows ≤5% loss over 20 hours of continuous operation, whereas bare CdS/CIGS shows a rapid degradation within the first 4 hours.

The need for sustainable energy sources has directed intensive research efforts to solar water splitting for the production of hydrogen.[1] To date, this strategy has largely been enabled by the use of inorganic semiconductor materials in photoelectrochemical (PEC) cells.[2] In this approach, incident light is absorbed by the semiconductor layer at the photocathode to generate electron–hole pairs, and these electrons are used to drive H_2O reduction. The performance of this process is determined by the semiconductor's bandgap, energy levels, and light absorption coefficient. The simultaneous achievement of high performance combined with stability is a grand challenge for photoelectrochemical water splitting.

Among various materials investigated as photocathodes, the Cu-chalcopyrite family has received considerable attention. This is due to their high absorption coefficients, high carrier mobilities and tunable band gap values (1.0–2.43 eV).[3,4] The conduction band of these semiconductors is particularly well positioned above the reduction potential of water, making them promising candidates for H_2 generation photocathodes.[5–8]

Within this family, $CuInGaS_2$ has received considerable attention as a photocathode for solar water splitting, given its high photocathode voltage, efficient light absorption, and outstanding optoelectronic properties.[9,10] Recently, n-type CdS was deposited onto $CuInGaS_2$ thin films to form a p–n junction to assist charge separation in PEC water splitting. Competitive photocurrents were demonstrated for the CdS and Pt modified $CuIn_{0.7}Ga_{0.3}S_2$ photocathodes for PEC water splitting.[11] Unfortunately, due to poor stability (<2 hours), the application of CdS/CIGS photoelectrodes has been limited.

The modification of CdS/CIGS materials using a stable but band-aligned protecting layer could fulfill the requirement for highly efficient water reduction materials.

Previous reports have demonstrated that n-type graphitic C_3N_4 (g-C_3N_4) possesses excellent photocatalytic activity for H_2 production from water splitting.[12] Its relatively low band-gap energy E_g (~2.7 eV) provided significant absorption of visible light, and the strong covalent bonds between carbon and nitrogen atoms led to a high chemical stability under acidic and basic conditions.[13,14]

Attempts to incorporate g-C_3N_4 into heterostructured complexes (g-C_3N_4/$CuInS_2$) have been shown to produce stable photocurrent generation.[15] However, in this approach, g-C_3N_4 did not contribute to photocatalytic activity, and no significant improvements in performance were observed.

The controlled doping of g-C_3N_4 with suitable anions such as sulfur (S) has been reported as a means to tune its electronic structure *via* quantum confinement effects. In this way, the energetics, light absorption, and photoreactivity of g-C_3N_4 can be tailored.[16–19]

We took the view that S doping could be used as a powerful tool to tailor the optoelectronic and photochemical properties of g-C_3N_4. We posited that the incorporation of this engineered

[a]Department of Physics, East China University of Science & Technology, 130 Meilong Road, Shanghai 200237, China. E-mail: bo.zhang@ecust.edu.cn; jhzhong@ecust.edu.cn

[b]Key Laboratory for Ultrafine Materials of Ministry of Education, School of Materials Science and Engineering, East China University of Science & Technology, 130 Meilong Road, Shanghai 200237, China

[c]Department of Electrical and Computer Engineering, University of Toronto, 35 St George Street, Toronto, Ontario M5S 1A4, Canada

[d]Department of Mechanical and Industrial Engineering, University of Toronto, 5 King's College Road, Toronto, Ontario M5S 3G8, Canada

[e]Laboratory of Advanced Materials, Department of Chemistry, Collaborative Innovation Center of Chemistry for Energy Materials, Fudan University, 2005 Song-Hu Road, Shanghai, 200433, China

† Electronic supplementary information (ESI) available: Experimental methods and supporting figures. See DOI: 10.1039/c6ta10222k

layer into $C_3N_{4-x}S_{3x/2}$/CdS/CIGS heterocomposites could potentially result in (i) an optimally aligned energy landscape that increases photocatalytic activity, (ii) a superior electrochemical stability, and, (iii) a protective layer that prevents CdS segregation into the electrolyte.

Herein we report the design and fabrication of $C_3N_{4-x}S_{3x/2}$/CdS/CIGS heterojunctions that achieve efficient PEC water reduction. Their record photocurrent (-5 mA cm^{-2} at -0.3 V *vs.* the RHE) and stability (up to 20 h) represent a new record for CdS/CIGS composites in neutral electrolytes without co-catalysts.

The energy band structure of the $C_3N_{4-x}S_{3x/2}$/CdS/CIGS heterojunction and the proposed mechanism of PEC water oxidation are shown in Fig. 1a. Excited electrons in the CIGS are driven toward $C_3N_{4-x}S_{3x/2}$ through CdS. Photogenerated holes from the $C_3N_{4-x}S_{3x/2}$ layer migrate to the surface of CIGS due to favorable band alignment. Thus, the $C_3N_{4-x}S_{3x/2}$/CdS/CIGS heterojunction photocathode can potentially improve efficient charge separation across the favorable band structure to enable PEC hydrogen evolution.

The morphologies of CIGS and modified-CIGS electrodes (CdS/CIGS and $C_3N_{4-x}S_{3x/2}$/CdS/CIGS) were analyzed using top-view scanning electron microscopy and energy dispersive X-ray fluorescence spectroscopy (SEM–EDX) (Fig. 1b, c and S1†). Rough surface features are observed for CIGS (Fig. 1b), in accordance with previous literature.[11] The surface of each CIGS grain is partially covered with small CdS particles, in contrast to the surface image of bare CIGS (Fig. 1c). After the deposition of $C_3N_{4-x}S_{3x/2}$, CdS/CIGS grain boundaries are covered, delivering efficient protection of CdS from corrosion during PEC measurement (Fig. S1†).

To assess further the presence of $C_3N_{4-x}S_{3x/2}$, energy dispersive spectroscopy (EDS) was conducted (Fig. S1†). This revealed that C, N and S elements can be observed on the top of the $C_3N_{4-x}S_{3x/2}$/CdS/CIGS film. Typical TEM images of C_3N_4 and $C_3N_{4-x}S_{3x/2}$ particles were also examined (see Fig. S3†). XRD patterns of each of the various samples were obtained to ascertain the crystalline structure of the CIGS, CdS/CIGS and $C_3N_{4-x}S_{3x/2}$/CdS/CIGS samples (Fig. 2a). The four main peaks located at 28.3°, 32.9°, 46.9° and 55.6° in the four samples are assigned to the diffraction of the (112), (004)/(200), (204)/(220) and (116)/(312) planes of $CuInGaS_2$, respectively.[11] Peaks of the SnO_2 substrate (JCPDS no. 46-1088) were also observed in all samples. After the deposition of g-C_3N_4, the C_3N_4/CdS/CIGS exhibited the same crystal structure as that of the CIGS sample, indicating that no obvious change took place in the crystal structure of C_3N_4/CdS/CIGS. Moreover, the one distinct peak located at 27.5° was indexed to the $C_3N_{4-x}S_{3x/2}$/CdS/CIGS sample, showing a slight shift of 0.1° toward the pure g-C_3N_4 sample, in agreement with previous reports.[20]

According to the experimental characterization by Liu *et al.*,[16] C–S bonds are formed in the framework of C–N bonds by replacing N with S. The doping configurations are shown in Fig. 2b. The presence of $C_3N_{4-x}S_{3x/2}$ and different C-bonds was further confirmed using X-ray photoelectron spectroscopy (XPS) (Fig. 2c–f). All the binding energies were calibrated using adventitious carbon (C 1s) at 284.6 eV as a reference. By means

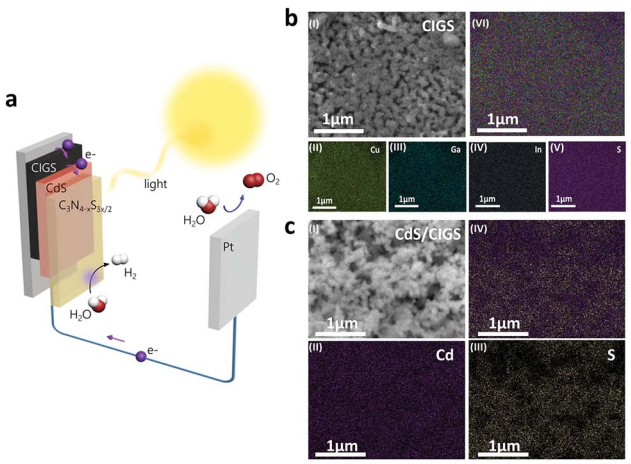

Fig. 1 (a) A three-dimensional energy band structure of the $C_3N_{4-x}S_{3x/2}$/CdS/CIGS heterojunction and the proposed mechanism of photoelectrochemical water oxidation. (b) Top-view SEM–EDX elemental mapping images showing the CIGS SEM image (I), Cu distribution (II), Ga distribution (III), In distribution (IV), S distribution (V), and superimposed distributions (VI). (c) Top-view SEM–EDX elemental mapping images showing the CdS/CIGS SEM image (I), Cd distribution (II), S distribution (III), and superimposed distributions (IV).

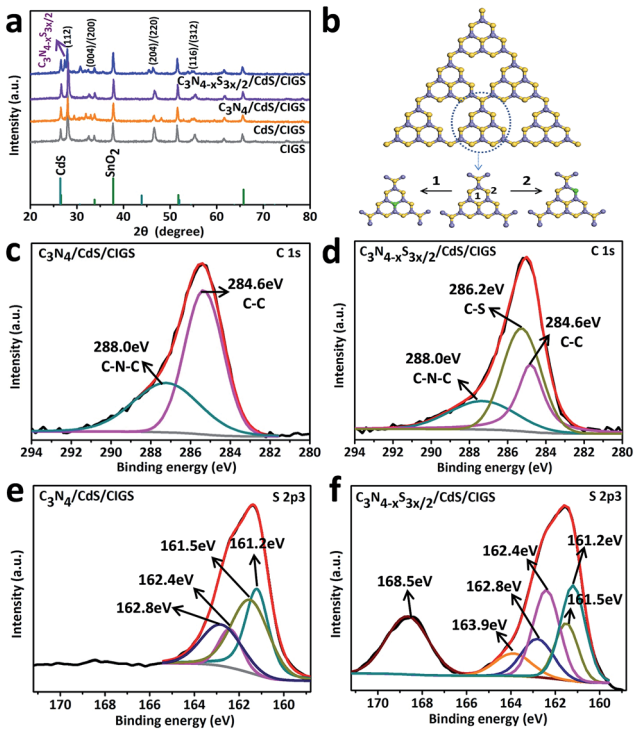

Fig. 2 (a) XRD spectrum of CIGS, CdS/CIGS, C_3N_4/CdS/CIGS and $C_3N_{4-x}S_{3x/2}$/CdS/CIGS photocathodes. (b) Atomic structure model of a perfect graphitic C_3N_4 sheet consisting of melem units, and schematic view of the doping sites (1 and 2). The C, N, and S atoms are depicted using purple, yellow, and green balls, respectively. (c–f) XPS spectra of C 1s for C_3N_4/CdS/CIGS (a) and $C_3N_{4-x}S_{3x/2}$/CdS/CIGS (b), and S 2p3 for C_3N_4/CdS/CIGS (c) and $C_3N_{4-x}S_{3x/2}$/CdS/CIGS (d) photocathodes.

of XPS-peak-differentiation-imitating analysis, two peaks at ~284.6 eV and ~288.0 eV were obtained in the C 1s peak of the C_3N_4/CdS/CIGS sample, and these can be assigned to C–N–C bonding and C–C bonding, respectively (Fig. 2c).[21] Another S 2p peak centered at ~286.2 eV was observed, and it is ascribed to the formation of C–S bonds[22] and confirms the existence of $C_3N_{4-x}S_{3x/2}$.

The remaining S peaks can be used to discern the different layers of the heterostructure (Fig. 2e). The S 2p3 peak was fit into six peaks at 161.2 eV, 161.5 eV, 162.4 eV, 162.8 eV, 163.9 eV and 168.5 eV. The binding energies of S $2p_{2/3}$ and S $2p_{1/2}$ at 161.5 and 162.8 eV, respectively, are ascribed to S^{2-} in the $CuIn_{0.7}Ga_{0.3}S_2$.[11] The peaks centered at 161.2 eV (S $2p_{3/2}$) and 162.4 eV (S $2p_{1/2}$) are consistent with S^{2-} in CdS.[23] The two S 2p peaks at 163.9 and 168.5 eV are analogous to the S 2p peaks of the pristine surface of $C_3N_{4-x}S_{3x/2}$.[22]

We then proceeded to investigate the PEC water reduction properties of the $C_3N_{4-x}S_{3x/2}$/CdS/CIGS photoanode. We measured the current density *versus* potential curves of pristine and modified CIGS electrodes under simulated sunlight (AM 1.5G) illumination (Fig. 3a). The photocurrent of a bare CIGS film was negligible (below -1.5 mA cm^{-2} at -0.3 V *vs.* the RHE). An appreciable enhancement of the photocurrent is achieved by the incorporation of a chemical-bath-deposited CdS layer to form a CdS/CIGS structure (-2 mA cm^{-2} at -0.3 V *vs.* the RHE), consistent with similar systems reported previously.[11] The dramatic improvement in photocathodic properties is ascribed to enhanced charge separation driven by the resulting p–n junction established between the CIGS and CdS layers.[24]

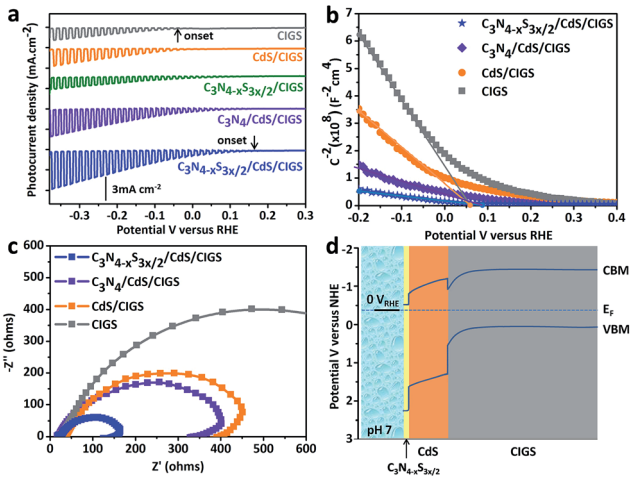

Fig. 3 (a) Current–potential plots of CIGS, CdS/CIGS, C_3N_4/CdS/CIGS and $C_3N_{4-x}S_{3x/2}$/CdS/CIGS photocathodes in a 1 M K_2HPO_4/KH_2PO_4 solution (pH = 7) irradiated with chopped AM 1.5G illumination. (b) Mott–Schottky plots of CIGS, CdS/CIGS, C_3N_4/CdS/CIGS and $C_3N_{4-x}S_{3x/2}$/CdS/CIGS photocathodes. The AC amplitude is 10 mV and the frequency is 200 Hz. (c) Electrochemical impedance spectroscopy of CIGS, CdS/CIGS, C_3N_4/CdS/CIGS and $C_3N_{4-x}S_{3x/2}$/CdS/CIGS photocathodes under Xe lamp illumination. Electrolyte: 1 M K_2HPO_4/KH_2PO_4 solution (pH = 7). Potential: 0 V_{RHE}. (d) The schematic band diagram at the electrolyte–electrode interface for the $C_3N_{4-x}S_{3x/2}$/CdS/CIGS electrode at 0 V_{RHE}.

After the deposition of C_3N_4, the photocurrent was further increased compared to that of CdS/CIGS films. The optimized $C_3N_{4-x}S_{3x/2}$ layer accounts for the large improvement in current density achieved, reaching -5 mA cm^{-2} at -0.3 V *vs.* the RHE. This current density is three times higher than that of a bare CIGS film. We attribute this to the facilitation of hole–electron separation and charge transfer using CdS and $C_3N_{4-x}S_{3x/2}$.

The benefits of the $C_3N_{4-x}S_{3x/2}$/CdS/CIGS heterojunction are also observed in the onset potentials. Positively shifted onset potentials (+0.2 V) for water reduction are observed in all samples modified with C_3N_4 or $C_3N_{4-x}S_{3x/2}$.

To ascertain the role of the $C_3N_{4-x}S_{3x/2}$, we had investigated its electrocatalytic activity over $C_3N_{4-x}S_{3x/2}$ and C_3N_4 for water reduction, and the results are showed in Fig. S6.† It shows that $C_3N_{4-x}S_{3x/2}$ produces a current density of 1 mA cm^{-2} at an overpotential (η) of ~680 mV, whereas C_3N_4 produces the same current density at a much higher η (750 mV), indicating that there is almost no catalytic activity. And the role of the $C_3N_{4-x}S_{3x/2}$ can be considered as a selective layer that collects electrons.

To further verify the role of the $C_3N_{4-x}S_{3x/2}$, we have prepared CdS/Cu(In,Ga)S_2 using a chemical vapor deposition (CVD) route. The results are shown in Fig. S7.† The photocurrent delivered by the best-performing electrodes attains a value of 4.5 mA cm^{-2} for the $C_3N_{4-x}S_{3x/2}$/CdS/CIGS photocathode – at 0 V *versus* the RHE, which is almost ten times that of the CdS/CIGS photocathode without $C_3N_{4-x}S_{3x/2}$. Nevertheless, we further assessed the stability of the hybrid photocathodes which were prepared with the CdS/CIGS substrate using a chemical vapor deposition (CVD) route. Stability measurements were conducted using chronoamperometry at the same fixed potential of 0 V *versus* the RHE. The $C_3N_{4-x}S_{3x/2}$/CdS/CIGS electrode showed a rapid loss over a few minutes of operation. Therefore, we believe that the large photocurrent of the CVD electrode should be contributed to electrode corrosion rather than water reduction. And in this regard, we chose the CdS/CIGS substrate prepared using a wet chemical route and abandoned the chemical vapor deposition (CVD) route in the original manuscript.

We then sought to perform a mechanistic study to understand how a $C_3N_{4-x}S_{3x/2}$ overlayer improves the photocathode performance in different phases. The enhanced heterojunction not only reduces surface charge recombination otherwise occurring in CdS, but it also increases the accumulation of electrons at the electrode surface. This result is consistent with the Mott–Schottky analysis (Fig. 3b) wherein the onset potential of the $C_3N_{4-x}S_{3x/2}$/CdS/CIGS is 200 mV more positive than that of CIGS. We have calculated the donor densities according to the following equation: $N_d = (2/e_o\varepsilon\varepsilon_o)[d(1/C^2)/dV]^{-1}$, where e_o is the electron charge, ε is the dielectric constant, ε_o is the permittivity of vacuum, N_d is the dopant density, and C is the capacitance derived from the electrochemical impedance obtained at each potential (V) with a 200 Hz frequency. With an ε value of *ca.* 10 for $CuInGaS_2$,[25–27] the donor density of $C_3N_{4-x}S_{3x/2}$/CdS/CIGS, C_3N_4/CdS/CIGS, CdS/CIGS and CIGS electrodes is calculated to be 8.4×10^{19}, 2.8×10^{19}, 1×10^{19} and 5.8×10^{18}, respectively. The hybrid exhibits a flatter Mott–Schottky plot compared to

CIGS and CdS/CIGS. The variation in the flat band induced by the change in the surface interfacial dipole with the different overlayers is what causes significant differences in the developed band bending for the same applied bias. The $C_3N_{4-x}S_{3x/2}$ accelerates in this way water reduction kinetics and facilitates charge transfer between the different layers of the hybrid. The Mott–Schottky plots of C_3N_4 and $C_3N_{4-x}S_{3x/2}$ photocathodes are showed in Fig. S8.† The variation of the Mott–Schottky plots is negligible after sulfur doping, which means that the carrier concentration and flat band potential of the C_3N_4 do not change after the sulfur-doping treatment.

We then carried out electrochemical impedance spectroscopy (EIS) measurements to investigate the interfacial charge transfer process (Fig. 3c). The semicircle at a low frequency is indicative of the interfacial charge transfer at the electrode/electrolyte interface.[28,29] The diameter of the semicircle becomes the smallest after the deposition of $C_3N_{4-x}S_{3x/2}$, proving that modification with $C_3N_{4-x}S_{3x/2}$ significantly enhances electron transfer by reducing the recombination of electron–hole pairs. We offer a schematic band diagram at the electrolyte–electrode interface for the $C_3N_{4-x}S_{3x/2}$/CdS/CIGS electrode at 0 V_{RHE} in Fig. 3d. From the UV-Vis plots of CIGS and CdS, the band gap energy determined by plotting $(\alpha h\nu)^2$ *versus* $h\nu$ was 1.51 eV and 2.42 eV respectively. For $C_3N_{4-x}S_{3x/2}$ and g-C_3N_4 the band gap energy determined by plotting $(\alpha h\nu)^{1/2}$ *versus* $h\nu$ was 2.75 eV and 2.80 eV respectively (Fig. S9†). In addition, the conduction band offset (CBO) of the CdS/CIGS junction was estimated to be *ca.* 0.45(±0.15) eV and 1.06(±0.15) eV for the VBO.[30] Such a cliff-type alignment is in agreement with several reports regarding the CdS/$CuInS_2$ heterojunction.[30–33] Moreover, the value of the VBM offset between CdS and $C_3N_{4-x}S_{3x/2}$ was 0.6eV (Fig. S12†).

These data, together with the band gap energy estimated from the UV-visible spectra, allow us to present the absolute energy scheme, including conduction band (CB) and valence band (VB) positions (Fig. 3d).

In sum, the matched energy levels of $C_3N_{4-x}S_{3x/2}$, CdS and CIGS facilitate photogenerated charge separation and transfer across the interfacial domains of the hierarchical heterojunction.

We then turned our attention to the optical properties of the hybrid materials and performed UV-Vis absorption spectroscopy measurements (Fig. 4a). The $C_3N_{4-x}S_{3x/2}$/CdS/CIGS electrode exhibits a higher absorption coefficient at wavelengths between 500 nm and 780 nm compared to other samples. This arises from the synergistic effect of $C_3N_{4-x}S_{3x/2}$ and CdS/CIGS. These findings confirm the enhanced light harvesting properties of $C_3N_{4-x}S_{3x/2}$ modified composites.

The incident photon-to-current efficiency (IPCE) values collected for various CIGS photocathodes as a function of wavelength under a bias of −0.4 V *vs.* the RHE are reported in Fig. 4b. The $C_3N_{4-x}S_{3x/2}$/CdS/CIGS electrode shows a dramatic improvement over the entire spectral range compared to the other three, with an IPCE of over 40% at wavelengths ranging from 400 to 700 nm. The IPCE decreases steeply at wavelengths longer than 700 nm, in agreement with the obtained bandgaps. The increased IPCE value for the $C_3N_{4-x}S_{3x/2}$ correlates the

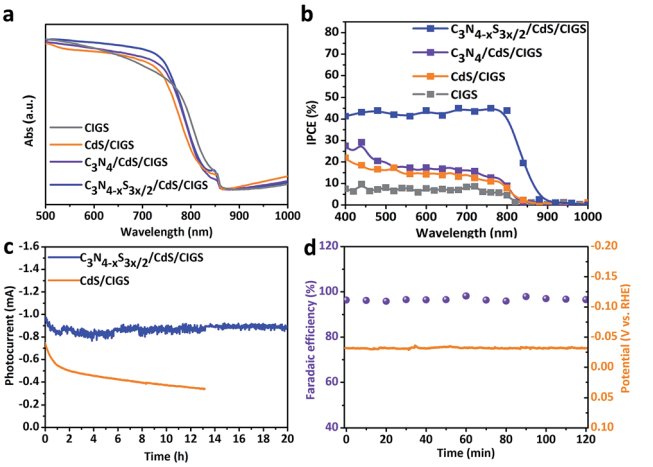

Fig. 4 (a) UV-Vis absorption spectra of CIGS, CdS/CIGS, C_3N_4/CdS/CIGS and $C_3N_{4-x}S_{3x/2}$/CdS/CIGS. (b) Incident photon to current efficiency (IPCE) spectrum of CIGS, CdS/CIGS, C_3N_4/CdS/CIGS and $C_3N_{4-x}S_{3x/2}$/CdS/CIGS photocathodes in a 1 M K_2HPO_4/KH_2PO_4 solution (pH = 7) at −0.4 V_{RHE}. (c) Stability of CdS/CIGS and $C_3N_{4-x}S_{3x/2}$/CdS/CIGS photocathodes as indicated by the steady-state photocurrent characterization with a device held at 0 V *versus* the RHE under 100 mW cm^{-2} illumination in 1 M K_2HPO_4/KH_2PO_4 solution (pH = 7). (d) Chronopotentiometric curves obtained with the $C_3N_{4-x}S_{3x/2}$/CdS/CIGS photocathode with constant current densities of 1 mA cm^{-2}, and the corresponding faradaic efficiency from gas chromatography measurement of evolved H_2.

enhanced absorption with the improved charge separation that gives rise to the observed increase in PEC performance.

Lastly, we assessed the stability of the hybrid photocathodes. Stability measurements were conducted using chronoamperometry at a fixed potential of 0 V *versus* the RHE. The $C_3N_{4-x}S_{3x/2}$/CdS/CIGS electrode shows ≤5% loss over 20 hours of operation (Fig. 4c), and this surpasses the stability of previously reported CdS/CIGS photocathodes.[11,33] The chronopotentiometric curves obtained at a constant current density of 1 mA cm^{-2} and the corresponding faradaic efficiency for H_2 evolution reveal an efficiency (96%) that closely approaches unity (Fig. 4d). The quantitative analyses of the dissolved Cd in 1 M K_2HPO_4/KH_2PO_4 solution after 20 h of operation of the CdS/CIGS and $C_3N_{4-x}S_{3x/2}$/CdS/CIGS photocathodes were performed using ICP-MS (see Table S2†). These confirm that the $C_3N_{4-x}S_{3x/2}$/CdS/CIGS heterocomposites result in a protective layer that prevents CdS segregation into the electrolyte.

Conclusions

We have demonstrated a new and efficient photocathode for solar water splitting. An n-type $C_3N_{4-x}S_{3x/2}$ layer deposited on a CdS/CIGS photocathode significantly enhances its PEC water splitting performance, including providing a higher photocurrent density and an improved onset potential. This strategy also results in unprecedented long-term stability in this material system. Detailed characterization shows that the $C_3N_{4-x}S_{3x/2}$ layer synergistically interacts with the CdS/CIGS layer, facilitating improved charge transport and enhancing light

harvesting, and also acting as a protective layer that avoids contact between the outer electrolyte solution and the CdS layer. These findings pave the way for hybrid photoelectrodes that combine high performance and stability for solar fuel devices.

Acknowledgements

This work was supported by the National Natural Science Foundation of China (21503079, 21573068 and 21373083) and Shanghai Municipal Natural Science Foundation (14ZR1410200).

Notes and references

1 (*a*) T. Hisatomi, J. Kubota and K. Domen, *Chem. Soc. Rev.*, 2014, **43**, 7520; (*b*) M. G. Walter, E. L. Warren, J. R. McKone, S. W. Boettcher, Q. Mi, E. A. Santori and N. S. Lewis, *Chem. Rev.*, 2010, **110**, 6446.
2 F. Jiang, Gunawan, T. Harada, Y. Kuang, T. Minegishi, K. Domen and S. Ikeda, *J. Am. Chem. Soc.*, 2015, **137**, 13691.
3 S. Merdes, D. Abou-Ras, R. Mainz, R. Klenk, M. Ch. Lux-Steiner, A. Meeder, H. W. Schock and J. Klaer, *Prog. Photovoltaics*, 2013, **21**, 88.
4 A. Ennaoui, M. Bärlz, J. Klaer, T. Kropp, R. Sáez-Araoz and M. Ch. Lux-Steiner, *Prog. Photovoltaics*, 2006, **14**, 499.
5 A. Fernandez, N. Dheree, J. Turner, A. Martínez, L. Arriaga and U. Cano, *Sol. Energy Mater. Sol. Cells*, 2005, **85**, 251.
6 B. Marsen, B. Cole and E. L. Miller, *Sol. Energy Mater. Sol. Cells*, 2008, **92**, 1054.
7 D. Yokoyama, T. Minegishi, K. Maeda, M. Katayama, J. Kubota, A. Yamada, M. Konagai and K. Domen, *Electrochem. Commun.*, 2010, **12**, 851.
8 S. Ikeda, T. Nakamura, S. M. Lee, T. Yagi, T. Harada, T. Minegishi and M. Matsumura, *ChemSusChem*, 2011, **4**, 262.
9 S. Ikeda, M. Nonogaki, W. Septina, G. Gunawan, T. Harada and M. Matsumura, *Catal. Sci. Technol.*, 2013, **3**, 1849.
10 Q. Li, L. Zhai, C. Zou, X. Huang, L. Zhang, Y. Yang, X. Chen and X. Huang, *Nanoscale*, 2013, **5**, 1638.
11 Z. Guan, W. Luo, J. Feng, Q. Tao, Y. Xu, X. Wen, G. Fu and Z. Zou, *J. Mater. Chem. A*, 2015, **3**, 7840.
12 J. Liu, Y. Liu, N. Liu, Y. Han, X. Zhang, H. Huang, Y. Lifshitz, S. T. Lee, J. Zhong and Z. Kang, *Science*, 2015, **347**, 970.
13 G. P. Dong, Y. H. Zhang, Q. W. Pan and J. R. Qiu, *J. Photochem. Photobiol., C*, 2014, **20**, 33.
14 G. Chen and S. H. Gao, *Chin. Phys.*, 2012, **21**, 107101.
15 F. Yang, V. Kuznietsov, M. Lublow, C. Merschjann, A. Steigert, J. Klaer, A. Thomase and T. Schedel-Niedrig, *J. Mater. Chem. A*, 2013, **1**, 6407.
16 G. Liu, P. Niu, C. Sun, S. C. Smith, Z. Chen, G. Q. Lu and H. M. Cheng, *J. Am. Chem. Soc.*, 2010, **132**, 11642.
17 J. S. Zhang, J. H. Sun, K. Maeda, K. Domen, P. Liu, M. Antonietti, X. Z. Fu and X. C. Wang, *Energy Environ. Sci.*, 2011, **4**, 675.
18 J. Hong, X. Xia, Y. Wang and R. Xu, *J. Mater. Chem.*, 2012, **22**, 15006.
19 Y. J. Cui, J. S. Zhang, G. G. Zhang, J. H. Huang, P. Liu, M. Antonietti and X. C. Wang, *J. Mater. Chem.*, 2011, **21**, 13032.
20 J. Xu, S. Cao, T. Brenner, X. Yang, J. Yu, M. Antonietti and M. Shalom, *Adv. Funct. Mater.*, 2015, **25**, 6265.
21 J. Hou, H. Cheng, O. Takedab and H. Zhu, *Energy Environ. Sci.*, 2015, **8**, 1348.
22 S. A. Wohlgemuth, R. J. White, M. G. Willinger, M. M. Titiricia and M. Antoniettia, *Green Chem.*, 2012, **14**, 1515.
23 L. J. Zhang, R. Zheng, S. Li, B. K. Liu, D. J. Wang, L. L. Wang and T. F. Xie, *ACS Appl. Mater. Interfaces*, 2014, **6**, 13406.
24 M. Malizia, B. Seger, I. Chorkendorff and P. C. K. Vesborg, *J. Mater. Chem. A*, 2014, **2**, 6847.
25 P. W. Li, R. A. Anderson and R. H. Plovnick, *J. Phys. Chem. Solids*, 1979, **40**, 333.
26 R. Marquez and C. Rincon, *Phys. Status Solidi B*, 1995, **191**, 115.
27 S. Chichibu, S. Shirakata, S. Isomura and H. Nakanishi, *Jpn. J. Appl. Phys., Part 1*, 1997, **36**, 1703.
28 S. K. Mohapatra, S. E. John, S. Banerjee and M. Misra, *Chem. Mater.*, 2009, **21**, 3048.
29 A. Mao, K. Shin, J. K. Kim, D. H. Wang, G. Y. Han and J. H. Park, *ACS Appl. Mater. Interfaces*, 2011, **3**, 1852.
30 L. Weinhardt, O. Fuchs, D. Groß, G. Storch, E. Umbach, N. G. Dhere, A. A. Kadam, S. S. Kulkarni and C. Heske, *Appl. Phys. Lett.*, 2005, **86**, 062109.
31 Y. Hashimoto, K. Takeuchi and K. Ito, *Appl. Phys. Lett.*, 1995, **67**, 980.
32 R. Scheer, *Prog. Photovoltaics*, 2012, **20**, 507.
33 W. Septina, Gunawan, S. Ikeda, T. Harada, M. Higashi, R. Abe and M. Matsumura, *J. Phys. Chem. C*, 2015, **119**, 8576.